# Mixed-Metal Monophosphate Tungsten Bronzes Containing Rhodium and Iridium

Alexander Karbstein,[a] Markus Weber,[a] Dominic Lahr,[a] Jörg Daniels,[a] Wilfried Assenmacher,[a] Werner Mader,[a] Frank Rosowski,[b] Stephan A. Schunk,[c] and Robert Glaum*[a]

Solution combustion synthesis followed by annealing in air led to the MPTB-related phosphates $(Rh_{1/6}W_{5/6}O_3)_8(PO_2)_4$, $(Ir_{1/6}W_{5/6}O_3)_8(PO_2)_4$ ($a = 5.258(2)$ Å, $b = 6.538(3)$ Å, $c = 17.322(8)$ Å), $(Rh_{1/9}W_{8/9}O_3)_{12}(PO_2)_4$ and $(Rh_{2/21}W_{19/21}O_3)_{14}(PO_2)_4$. Single-crystals of the mixed-metal (Rh,W)-MPTBs at $m = 4$ and at $m = 7$ were grown by chemical vapor transport (CVT). Their crystal structures have been refined from X-ray single-crystal data {**(Rh,W)-MPTB at $m = 4$**: $P2_12_12_1$, $Z = 1$, $a = 5.2232(3)$ Å, $b = 6.4966(3)$ Å, $c = 17.3819(9)$ Å, $R_1 = 0.032$, $wR_2 = 0.075$ for 1714 unique reflections, 1524 with $F_o > 4\sigma(F_o)$, 66 variables, 1 constraint, composition from refinement $(Rh_{0.15}W_{0.85}O_3)_8(PO_2)_4$; **(Rh,W)-MPTB at $m = 7$**: $P2_1/n$, $Z = 1$, $a = 5.2510(4)$ Å, $b = 6.4949(5)$ Å, $c = 26.685(2)$ Å, $\beta = 90.30(1)°$, $R_1 = 0.060$, $wR_2 = 0.163$ for 2074 unique reflections, 1894 with $F_o > 4\sigma(F_o)$, 100 variables, comp. from ref. $(Rh_{0.07}W_{0.93}O_3)_{14}(PO_2)_4$}. These structure refinements show unexpected distribution of Rh and W over the available metal sites. Further characterization (powder reflectance and magnetic measurements) of the (Rh,W)-MPTB at $m = 4$ and at $m = 7$ suggest for both phases a homogeneity range with respect to the Rh/W ratio and the presence of small amounts of $W^{5+}$ besides $Rh^{3+}$ and $W^{6+}$. Results of the ligand field analysis for the reference material $Rh(PO_3)_3$, which is containing the octahedral chromophore $[Rh^{III}O_6]$, are reported ($\Delta_o = 23200\ cm^{-1}$, $B = 490\ cm^{-1}$).

## Introduction

Thermodynamically metastable, multinary tungsten phosphates with $ReO_3$-like XRPD-pattern containing platinum group metals have recently been identified as catalyst materials for the formation of maleic anhydride via selective oxidation of *n*-butane.[1] Annealing these catalyst materials at temperatures above 900 °C leads to phases with XRPD pattern resembling those of phosphate tungsten bronzes (PTBs). These mixed-metal PTBs are expected to contain platinum group metals (PGM) in well-established chemical environments, which should lead, following the reasoning of the concepts of single-site catalysts and site isolation,[2] to even better catalyst performance than that observed for the disordered solids with $ReO_3$-like XRPD-pattern. Furthermore, up to now only a few anhydrous phosphates of rhodium and iridium have been characterized crystallographically ($RhPO_4$ and $Rh(PO_3)_3$,[3] $Ir(PO_3)_3$[4]). For this reason further characterization of PGM-containing mixed-metal MPTBs appeared of additional interest.

Since the discovery of the first tungsten bronze $A_xWO_3$ (*A*: Na, K) with yellow-golden color and metallic luster by Wöhler in 1825,[5] a wide range of bronzes containing transition metals have been studied.[6] Their structures consist of corner-sharing $MO_6$ octahedra arranged in a 3D-network, which can be interpreted as a distorted $ReO_3$-type structure. The interstitial position can be occupied by a large cation *A* to build a perowskite-type structure, which leads to mixed-valency tungsten (V,VI) and, as a result, interesting physical properties (e.g. electrical conductivity, antiferromagnetic ordering or superconductivity at low temperatures).[7,8]

Raveau et al. synthesized phosphate tungsten bronzes (PTB), where $ReO_3$-like slabs of $WO_6$ octahedra are separated by phosphate ($PO_4$) or diphosphate ($P_2O_7$) groups. These phosphates can be grouped into three classes of PTBs according to their structural features: the monophosphate tungsten bronzes with pentagonal tunnels ($MPTB_p$) and the general formula $(WO_3)_{2m}(PO_2)_4$ with $2 \le m \le 14$, the monophosphate tungsten bronzes with hexagonal tunnels ($MPTB_h$) $A_x(PO_2)_4(WO_3)_{2m}$ (*A*: Na, K, Pb) with $4 \le m \le 10$ and the diphosphate tungsten bronzes (DPTB) $A_x(P_2O_4)_2(WO_3)_{2m}$ (*A*: K, Rb, Ba, Tl) and $4 \le m \le 10$.[9] Note, that the *A*-site is not necessarily required to be occupied by a cation. It can be empty, thus leading to pure mixed-valent tungsten phosphates.

[a] *A. Karbstein, M. Weber, D. Lahr, Dr. J. Daniels, Dr. W. Assenmacher, Prof. Dr. W. Mader, Prof. Dr. R. Glaum*
*Institut für Anorganische Chemie*
*Rheinische Friedrich-Wilhelms-Universität Bonn*
*Gerhard-Domagk-Str. 1, D-53121 Bonn (Germany)*
*E-mail: rglaum@uni-bonn.de*
https://www.glaum.chemie.uni-bonn.de/arbeitsgruppe/mitarbeiter/glaum

[b] *Dr. F. Rosowski*
*BasCat - UniCat BASF JointLab, Technische Universität Berlin, 10623 Berlin, Germany*
*E-mail: frank.rosowski@basf.com*
https://www.bascat.tu-berlin.de/bascat/menue/about_us/scientific_directors/

[c] *Dr. S. A. Schunk*
*hte GmbH, Kurpfalzring 104, 69123 Heidelberg, Germany*
*E-mail: stephan.schunk@hte-company.de*
https://www.hte-company.com/

*Supporting information for this article is available on the WWW under https://doi.org/10.1002/ejic.202100047*

In particular, the $MPTB_p$ phases with their electronic structure are of interest, because they show phase transitions at low temperatures, which may lead to superconductivity and charge localization effects (charge density waves). An investigation of $(WO_3)_{14}(PO_2)_4$ ($m=7$) shows two phase transitions at $T_1=188$ K and $T_2=60$ K. These are related to Peierls distortions leading to charge density wave states and superconductivity below $T<0.3$ K.[8]

Substitution of tungsten(V) in the $ReO_3$-like slabs by other transition metals is possible. It is already known, that $W^{5+}$ can be replaced by appropriate combinations of tungsten(VI) with $M^{IV}$ or $M^{III}$ according to $M^{IV}_{1/2}W^{VI}_{1/2}$ and $M^{III}_{1/3}W^{VI}_{2/3}$, respectively. For the MPTB $(WO_3)_4(PO_2)_4$ ($m=2$) mixed-metal substitution variants with $M$: $V^{III,\,IV}$, $Cr^{III}$, $Fe^{III}$, $Mo^{III,\,IV}$ and $Ti^{IV}$ have been reported.[10] In addition to the described MPTBs at $m=2$, for $M$: Sc, V, Cr, Fe, Mo, Ru, Rh, In and Ir the ortho-pyrophosphates $M^{III}(WO_2)_2(P_2O_7)(PO_4)$ of identical sum formula (with respect to the MPTBs) but different structure were obtained.[10]

In this paper we report on synthesis, thermal behavior and characterization of several mixed-metal (Rh,W)- and (Ir,W)-MPTBs. For characterization results from XRPD, SXRD, electron microscopy, UV/vis-spectroscopy, and magnetic measurements are presented.

## Results and Discussion

### Synthesis

The new mixed-metal (mm) MPTBs $(Rh_{1/6}W_{5/6}O_3)_8(PO_2)_4$, $(Rh_{1/9}W_{8/9}O_3)_{12}(PO_2)_4$, $(Rh_{2/21}W_{19/21}O_3)_{14}(PO_2)_4$ and $(Ir_{1/6}W_{5/6}O_3)_8(PO_2)_4$ have been obtained as single-phase, micro-crystalline powders (XRPD) by solution combustion synthesis (SCS)[11] followed by annealing of the combustion products in air. For SCS $Rh(NO_3)_3$ (Umicore, Hanau) or $Ir(acac)_3$ (Umicore, Hanau), $(NH_4)_6W_{12}O_{39}\cdot(H_2O)_{4.8}$ (Alfa Aesar, Karlsruhe), $H_3PO_4$ (VWR, Darmstadt), and the polydentate ligand glycine (Labochem International, Heidelberg) were dissolved in water (molar ratio metal : glycine = 1 : 3). Conc. $HNO_3$ (Fisher Scientific, Schwerte) in excess was added as oxidant to the solution to prevent the reduction of rhodium or iridium during the combustion. To our observation, formation of the PGM metals is irreversible under the described reaction conditions and has to be avoided. The solutions were evaporated at temperatures $\vartheta \leq 100\,^{\circ}C$ and thereafter ignited in a preheated furnace at $\vartheta = 400\,^{\circ}C$, where a self-propagating combustion took place and yielded black, voluminous, amorphous (XRPD) powders. These intermediates were ground and annealed in air with stepwise rising of the temperature up to 1000 °C for $(Rh_{1/6}W_{5/6}O_3)_8(PO_2)_4$ and $(Ir_{1/6}W_{5/6}O_3)_8(PO_2)_4$ and up to 1100 °C for $(Rh_{1/9}W_{8/9}O_3)_{12}(PO_2)_4$ and $(Rh_{2/21}W_{19/21}O_3)_{14}(PO_2)_4$. Thus obtained powders display a dark-green color for the rhodium and black for the iridium compounds. XRPD pattern were recorded after each annealing step to control the progress of product formation until the thermodynamically stable mm-MPTB phase was obtained single-phase (see XRPD pattern in Figure 1 and Figures S1-S4). In case of $(Rh_{1/9}W_{8/9}O_3)_{12}(PO_2)_4$ the described procedure led always to $(Rh_{2/21}W_{19/21}O_3)_{14}(PO_2)_4$ as minor by-phase. We attribute this outcome to the close proximity of chemical composition of the two compounds and the rather small amounts of material used for synthesis, due to the high cost of rhodium.

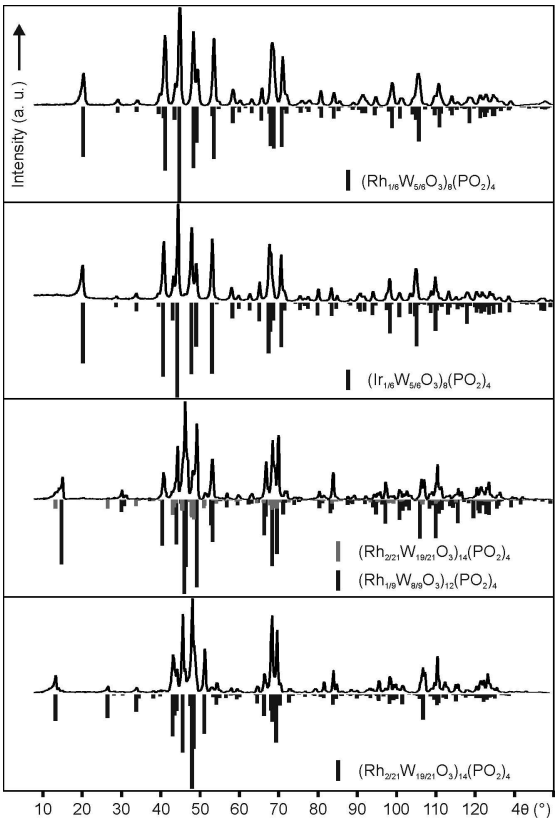


**Figure 1.** XRPD pattern (*IP* Guinier technique, Cu-$K_{\alpha 1}$) of $(Rh_{1/6}W_{5/6}O_3)_8(PO_2)_4$ (top) and $(Rh_{2/21}W_{19/21}O_3)_{14}(PO_2)_4$ (bottom) with simulations based on SXRD data. $(Ir_{1/6}W_{5/6}O_3)_8(PO_2)_4$ and $(Rh_{1/9}W_{8/9}O_3)_{12}(PO_2)_4$ (middle) with a simulation based on $(Rh_{2/21}W_{19/21}O_3)_{14}(PO_2)_4$ (grey) and $(WO_3)_8(PO_2)_4$[14] or $(WO_3)_{12}(PO_2)_4$[15] (black) with an even distribution of rhodium/iridium over all three tungsten sites.

Experiments aiming at "$(Rh_{2/9}W_{7/9}O_3)_6(PO_2)_4$" ($m=3$), "$(Rh_{2/15}W_{13/15}O_3)_{10}(PO_2)_4$" ($m=5$) or "$(Rh_{1/12}W_{11/12}O_3)_{16}(PO_2)_4$" ($m=8$) led to the neighboring MPTB phases. In case of iridium only $(Ir_{1/6}W_{5/6}O_3)_8(PO_2)_4$ was formed. The mixed-metal MPTBs $(M_{1/3}W_{2/3}O_3)_4(PO_2)_4$ ($m=2$) with $M$ = Rh, Ir were never observed. Instead, formation of $M(WO_2)_2(P_2O_7)(PO_4)_2$ ($M$ = Rh, Ir) did occur, as previously described by Roy et al.[12]

Lattice parameters of the MPTBs were determined using the program SOS[13] and $\alpha$-$SiO_2$ (Merck, Darmstadt) as internal standard (see Table 1). Interestingly, the lattice parameters $a$ and $b$ which are parallel to the $ReO_3$-type slabs of the (Rh,W)-MPTBs are smaller compared to the pure tungsten MPTBs, whereas the parameter $c$ (perpendicular to the $ReO_3$-type slabs) is enlarged (Table 1).

**Table 1.** Lattice parameters from XRPD data of (Rh,W)- and (Ir,W)-MPTBs in comparison to the pure tungsten phosphates.

| Compound | *a* [Å] | *b* [Å] | *c* [Å] | *β* [°] |
|---|---|---|---|---|
| *m* = 4 (orthorhombic) | | | | |
| $(WO_3)_8(PO_2)_4$ [14] | 5.285(2) | 6.569(1) | 17.351(3) | |
| $(Rh_{1/6}W_{5/6}O_3)_8(PO_2)_4$ | 5.223(1) | 6.513(2) | 17.356(6) | |
| $(Rh_{0.15}W_{0.85}O_3)_8(PO_2)_4$ [a] | 5.2232(3) | 6.4966(3) | 17.3819(9) | |
| $(Ir_{1/6}W_{5/6}O_3)_8(PO_2)_4$ | 5.258(2) | 6.538(3) | 17.332(8) | |
| *m* = 6 (orthorhombic) | | | | |
| $(WO_3)_{12}(PO_2)_4$ [15][a] | 5.2927(7) | 6.5604(7) | 23.549(3) | |
| $(Rh_{1/9}W_{8/9}O_3)_{12}(PO_2)_4$ | 5.229(2) | 6.540(3) | 23.599(7) | |
| *m* = 7 (monoclinic) | | | | |
| $(WO_3)_{14}(PO_2)_4$ [16][a] | 5.291(1) | 6.557(2) | 26.654(8) | 90.19 |
| $(Rh_{2/21}W_{19/21}O_3)_{14}(PO_2)_4$ | 5.245(2) | 6.507(2) | 26.693(8) | 90.10(4) |
| $(Rh_{0.07}W_{0.93}O_3)_{14}(PO_2)_4$ [a] | 5.2510(4) | 6.4949(5) | 26.6854(19) | 90.30(1) |

[a] Lattice parameters from single-crystal measurement at room temperature (crystals from CVT, composition from structure refinement).

### Progress of phase formation and thermal decomposition

For $(Rh_{2/21}W_{19/21}O_3)_{14}(PO_2)_4$, the (Rh,W)-MPTB at *m* = 7, as representative example, the progress of phase formation starting from the amorphous intermediate obtained by SCS is summarized in Figure 2. It shows, rather unexpectedly, strong kinetic effects during phase formation. After SCS (400 °C ignition temperature; hot spot temperature up to 900 °C for a few seconds) the intermediate exhibits a diffraction pattern typical of an amorphous solid. Heating to 750 °C leads to less "amorphous background" and development of rather broad Bragg peaks indicating the formation of a thermodynamically metastable phase with a $ReO_3$-related pattern. The chemical composition of this phase, $(Rh_{2/21}W_{19/21}O_3)_{14}(PO_2)_4$, can be rewritten as $(Rh^{III}_{2/27}W^{VI}_{19/27}P^{V}_{6/27})(O_{25/9}\square_{2/9})$ to emphasize its relation to $ReO_3$ and to show the oxygen-deficiency as a consequence of the average oxidation state of the cations. This and related $ReO_3$-like phases are obtained with high reproducibility by the described protocol and they show remarkable thermal stability against transformation into the thermodynamically stable equilibrium phases. However, without SCS and initial annealing temperatures too high these phases were never obtained.

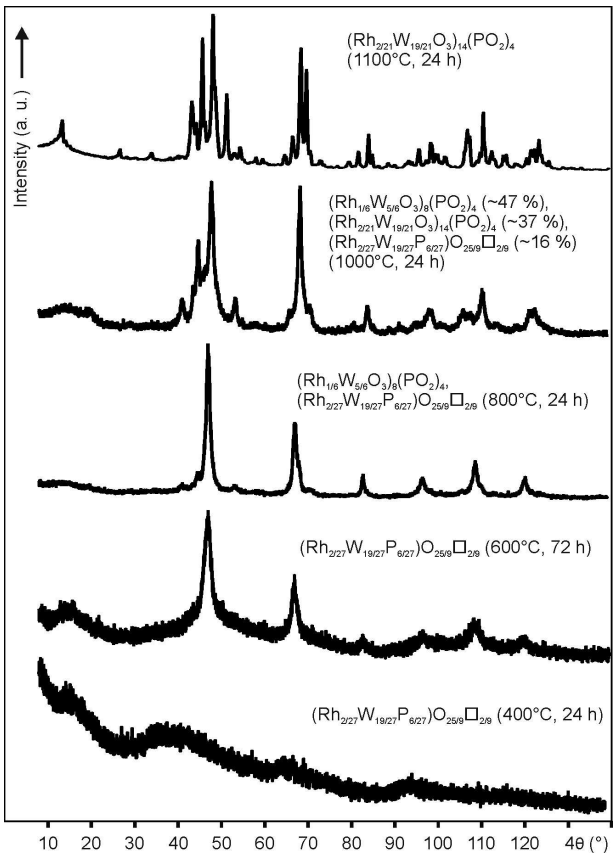


**Figure 2.** XRPD pattern (*IP* Guinier technique, Cu-$K_{\alpha 1}$) of $(Rh_{2/21}W_{19/21}O_3)_{14}(PO_2)_4$ after several consecutive steps of annealing starting with the combustion product from SCS, rel. amounts (wt %) estimated with MATCH!.[19]

Surprisingly, transformation (equilibration) of the single-phase homogenous $ReO_3$-like phase to the microcrystalline powder of $(Rh_{2/21}W_{19/21}O_3)_{14}(PO_2)_4$ (*m* = 7) does not occur directly, but via the apparently kinetically favorable formation of the (Rh,W)-MPTB at *m* = 4 (depleted in $WO_3$ with respect to the starting composition) and a $WO_3$-rich phase with $ReO_3$-related XRPD pattern. Thus, as can be taken from Figure 2, above 800 °C a pattern similar to $(WO_3)_8(PO_2)_4$ (MPTB at *m* = 4) begins to emerge from the amorphous background. Simultaneously, the lattice parameter *a* of the $ReO_3$-like phase shrinks slightly from 3.79 Å to 3.71 Å (see Table 2) and is thus approaching the value given in literature for cubic $WO_3$.[17] We are therefore relating this change to a depletion of the $ReO_3$-like phase of rhodium and phosphorus and an enrichment by $WO_3$. The powder obtained after annealing at 1000 °C (Figure 2) clearly shows, according to its XRPD pattern, an off-equilibrium mixture of three phases. The presence of the $WO_3$-rich, $ReO_3$-like phase (~16 %wt) and of the intermediate (Rh,W)-MPTB (*m* = 4; ~47 %wt), which has a higher content of rhodium and phosphorus than the starting mixture is apparently kinetically controlled. The equilibrium phase $(Rh_{2/21}W_{19/21}O_3)_{14}(PO_2)_4$ (*m* = 7) is already present in the mixture at ~37 %wt. Eventually, after annealing at 1100 °C the targeted (Rh,W)-MPTB at *m* = 7 is obtained as single-phase powder. Further heating up to 1200 °C of this (Rh,W)-MPTB in air leads to decomposition to $P_4O_{10}$ vapor, $WO_3$ (monoclinic after quenching to ambient temper-

**Table 2.** Lattice parameter *a* [Å] of the metastable intermediate phases with $ReO_3$-like XRPD pattern as a function of temperature [°C] during formation of the different (Rh,W)-MPTBs.

| | 600 | 700 | 750 | 800 | 1000 |
|---|---|---|---|---|---|
| $(Rh_{1/6}W_{5/6}O_3)_8(PO_2)_4$ | not det. | 3.786(8) | 3.783(7) | not det. | not det. |
| $(Rh_{1/9}W_{8/9}O_3)_{12}(PO_2)_4$ | 3.792(9) | 3.785(7) | not det. | 3.776(3) | 3.713(7) |
| $(Rh_{2/21}W_{19/21}O_3)_{14}(PO_2)_4$ | 3.780(5) | 3.781(6) | not det. | 3.776(4) | 3.718(7) |

ature), and rhodium (see Eq. 1). The latter two solid phases were identified by XRPD.

The progress of phase formation observed for the other mm-MPTBs under consideration, $(Rh_{1/6}W_{5/6}O_3)_8(PO_2)_4$, $(Ir_{1/6}W_{5/6}O_3)_8(PO_2)_4$ and $(Rh_{1/9}W_{8/9}O_3)_{12}(PO_2)_4$ is very similar to the one described for $(Rh_{2/21}W_{19/21}O_3)_{14}(PO_2)_4$ (see Tables S5-S7). However, there is variation in the temperature required to obtain the single-phase mm-MPTB and in their decomposition temperatures. Single-phase powders of $(Rh_{1/6}W_{5/6}O_3)_8(PO_2)_4$ and $(Ir_{1/6}W_{5/6}O_3)_8(PO_2)_4$ (both $m=4$) are formed already at about 800 °C, $(Rh_{1/9}W_{8/9}O_3)_{12}(PO_2)_4$ ($m=6$) around 1050 °C and $(Rh_{2/21}W_{19/21}O_3)_{14}(PO_2)_4$ ($m=7$) around 1100 °C. Short annealing periods of a few hours only slightly above their decomposition temperatures leads to stepwise loss of $P_4O_{10}$ and the formation of elementary rhodium and the (Rh,W)-MPTB with the next higher *m* (higher $WO_3$ content). Overall, the decomposition temperature of the (Rh,W)-MPTBs increases with decreasing content of rhodium/$P_4O_{10}$. This observation fits to the decomposition behavior of pure rhodium phosphates ($Rh(PO_3)_3$, $RhPO_4$), where the activity of $P_4O_{10}$ is higher and decomposition in air begins at 950 °C.[18]

$$3\ (Rh_{2/21}W_{19/21}O_3)_{14}(PO_2)_4(s) \rightarrow 38\ WO_3(s) + 4\ Rh(s) + 3\ P_4O_{10}(g) + 3\ O_2(g) \quad (1)$$

Based on their thermal decomposition temperatures and the assumption that $p(O_2)$ should exceed 0.2 bar for a detectable decomposition effect, an estimate of the thermodynamic data $\Delta_f H^0_{298}$, $S^0_{298}$, $C_p$ (coefficients A, B, C) of $(Rh_{1/6}W_{5/6}O_3)_8(PO_2)_4$ and $(Rh_{2/21}W_{19/21}O_3)_{14}(PO_2)_4$ was possible using the data of the binary oxides $Rh_2O_3$, $WO_3$ and $P_4O_{10}$. The estimation follows a procedure applied by *Schäfer* for $LaPO_4$.[20] For a summary of thermodynamic data used in the context of this paper, see Table S1.

## Crystallization by chemical vapor transport

Crystals of the (Rh,W)-MPTBs $(Rh_{1/6}W_{5/6}O_3)_8(PO_2)_4$ ($m=4$), $(Rh_{1/9}W_{8/9}O_3)_{12}(PO_2)_4$ ($m=6$) and $(Rh_{2/21}W_{19/21}O_3)_{14}(PO_2)_4$ ($m=7$) have been grown by chemical vapor transport (CVT)[21] in sealed silica tubes ($l=14$ cm, $d=1.5$ cm) with chlorine as transport agent. These show a dark greenish color, have edge lengths up to 300 $\mu$m and are isometric with a rectangular shape (Figure 3).

Pre-synthesized, single-phase powders (from SCS followed by annealing in air) were used as starting materials for CVT. Small amounts of $PtCl_2$ (~15 mg) were added for in situ generation of chlorine, the transport agent. Temperature gradients 950→900 °C for $(Rh_{1/6}W_{5/6}O_3)_8(PO_2)_4$ and 1090→1050 °C for $(Rh_{1/9}W_{8/9}O_3)_{12}(PO_2)_4$ and $(Rh_{2/21}W_{19/21}O_3)_{14}(PO_2)_4$ were applied. Ampoules were kept in the furnaces for 14 *d*. Under the given experimental conditions no decomposition of the (Rh,W)-MPTBs was observed. However, transport of $(Rh_{1/9}W_{8/9}O_3)_{12}(PO_2)_4$ and $(Rh_{2/21}W_{19/21}O_3)_{14}(PO_2)_4$ in the temperature gradient 950→900 °C led to deposition of $(Rh_{1/6}W_{5/6}O_3)_8(PO_2)_4$ in the sink due to non-stationary behavior of the system. For a general explanation of non-stationary transport behavior see.[21,22]

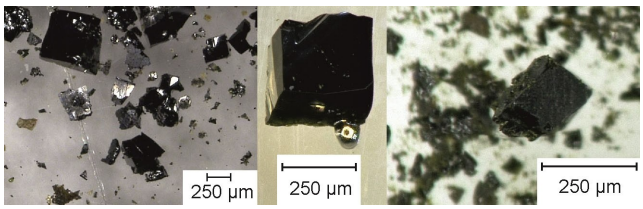


**Figure 3.** Crystals of $(Rh_{1/6}W_{5/6}O_3)_8(PO_2)_4$ (left, middle) and $(Rh_{2/21}W_{19/21}O_3)_{14}(PO_2)_4$ (right) obtained by CVT.

Chemical vapor transport of $(Rh_{1/6}W_{5/6}O_3)_8(PO_2)_4$ with chlorine as transport agent was modelled with the computer program CVTrans[23] using thermodynamic data given in Table S1. According to the modelling and in agreement with literature on CVT of $WO_3$ and $Rh_2O_3$ the transport active gas species are $WO_2Cl_2$, $RhCl_3$, $P_4O_{10}$, and $O_2$ (see Eq. 2).[18,21]

$$(Rh_{1/6}W_{5/6}O_3)_8(PO_2)_4(s) + 13/12\ Cl_2(g) \rightleftarrows 1/6\ RhCl_3(g) + 5/6\ WO_2Cl_2(g) + P_4O_{10}(g) + 13/24\ O_2(g) \quad (2)$$

## Crystal structure analyses

The (Rh,W)-MPTB at $m=4$ and $m=7$ are isotypic to their pure tungsten MPTB counterparts $(WO_3)_8(PO_2)_4$ ($P2_12_12_1$, $Z=1$)[14] and $(WO_3)_{14}(PO_2)_4$ ($P2_1/n$, $Z=1$).[16] Table 3 provides a summary on data collection and refinement of the crystal structures. Atomic coordinates and isotropic displacement parameters are shown in Table 4 and Table 5 (Anisotropic displacement parameters see Table S2 and Table S3). Refinements for both (Rh,W)-MPTB were hampered by twinning, cation disorder, and possibly stacking faults all of which are typical for monophosphate tungsten bronzes as has been pointed out in literature several times.[25] Due to the limited quality of the refinements we refrain from discussing interatomic distances (see Figures S8 and S9) in detail. Nevertheless, the distances are very similar to those observed for the pure MPTBs. The refinements do provide clear information on the metal sites with rhodium/tungsten mixed

**Table 3.** Summary on data collection and refinement of the crystal structures of $(Rh_{0.15}W_{0.85}O_3)_8(PO_2)_4$ and $(Rh_{0.07}W_{0.93}O_3)_{14}(PO_2)_4$.

| | | |
|---|---|---|
| Empirical formula | $Rh_{1.33}W_{6.67}P_4O_{32}$ | $Rh_{1.33}W_{12.67}P_4O_{50}$ |
| Structural formula | $(Rh_{0.167}W_{0.833}O_3)_8(PO_2)_4$ | $(Rh_{0.095}W_{0.905}O_3)_{14}(PO_2)_4$ |
| Refined formula | $(Rh_{0.146}W_{0.854}O_3)_8(PO_2)_4$ | $Rh_{1.04}W_{12.96}P_4O_{32}$ |
| Formula weight | 2012.40 | 3413.47 |
| Crystal system | orthorhombic | monoclinic |
| Space group | $P2_12_12_1$ (no. 19) | $P\,2_1/n$ (no. 14) |
| $T$ (K); $\lambda$ (Å) | 293(2); 0.71073 | 293(2); 0.71073 |
| $a$ (Å)[a] | 5.2232(3) | 5.2510(4) |
| $b$ (Å)[a] | 6.4966(3) | 6.4949(5) |
| $c$ (Å)[a] | 17.3819(9) | 26.6854(19) |
| β (°)[a] | 90 | 90.30(1) |
| $Z$ | 1 | 1 |
| $V$ (Å$^3$); $D_{calc}$ (g cm$^{-3}$) | 589.82(5); 5.665 | 910.09(12); 6.228 |
| Crystal dimensions (mm$^3$); color | 0.055 × 0.03 × 0.03; dark green | 0.068 × 0.042 × 0.021; dark green |
| $F$(0 0 0) | 874 | 1466 |
| Absorption | semi-empirical (multiscan)[24] | semi-empirical (multiscan)[24] |
| $\mu$ (mm$^{-1}$); ext. coef. | 33.648; 0.0026(2) | 40.453; 0 |
| Measured refls. ind. | 10119; 1714 | 7312; 2074 |
| No. of parameters | 58 | 100 |
| Theta range (°) | 3.35–29.91 | 3.05–27.59 |
| Index ranges | $-7 \le h \le 7$, $-9 \le k \le 9$, $-24 \le l \le 23$ | $-6 \le h \le 6$, $-7 \le k \le 8$, $-34 \le l \le 33$ |
| $GooF$ | 1.108 | 1.131 |
| $R_{int}$ | 0.0653 | 0.1217 |
| $R_1$ [$I > 2\sigma(I)$] | 0.0315 | 0.0600 |
| $R_1$; w$R_2$ (all data) | 0.0374; 0.0742 | 0.0649; 0.1687 |

[a] Lattice parameters from single-crystal measurement.

**Table 4.** $(Rh_{1/6}W_{5/6}O_3)_8(PO_2)_4$. Atomic coordinates and isotropic displacement parameters.

| Atom | $x$ | $y$ | $z$ | $s.o.f.$ | $U_{eq}$ [Å$^2$] |
|---|---|---|---|---|---|
| W1 | 0.2502(2) | 0.41042(6) | 0.04236(2) | 0.708(6) | 0.0142(2) |
| Rh1 | 0.2502(2) | 0.41042(6) | 0.04236(2) | 0.292(6) | 0.0142(2) |
| W2 | 0.25049(15) | 0.24727(5) | 0.37161(2) | 1 | 0.00929(12) |
| P | 0.2478(10) | 0.0604(3) | 0.18620(11) | 1 | 0.0079(4) |
| O1 | 0.963(2) | 0.2898(14) | 0.0006(6) | 1 | 0.018(2) |
| O2 | 0.213(3) | 0.2505(13) | 0.1383(5) | 1 | 0.026(2) |
| O3 | 0.228(2) | 0.1205(10) | 0.2701(4) | 1 | 0.016(2) |
| O4 | 0.033(2) | 0.0487(15) | 0.4064(5) | 1 | 0.017(2) |
| O5 | 0.532(2) | 0.1202(15) | 0.4044(5) | 1 | 0.018(2) |
| O6 | 0.549(2) | 0.399(2) | 0.3281(6) | 1 | 0.025(2) |
| O7 | 0.022(2) | 0.477(2) | 0.3288(6) | 1 | 0.022(2) |
| O8 | 0.281(2) | 0.4091(12) | 0.4599(4) | 1 | 0.021(2) |

occupancy. In addition, the refinements for both (Rh,W)-MPTB suggest slightly higher tungsten content than expected for the ideal compositions with rhodium(III) and tungsten(VI): $(Rh_{0.15}W_{0.85}O_3)_8(PO_2)_4$ instead of $(Rh^{III}_{1/6}W^{VI}_{5/6}O_3)_8(PO_2)_4$ ($m = 4$) and $(Rh_{0.07}W_{0.93}O_3)_{12}(PO_2)_4$ instead of $(Rh^{III}_{2/21}W^{VI}_{19/21}O_3)_{14}(PO_2)_4$ ($m = 7$); Table 3, Table 4, and Table 5. Details on the refinements are given in the Experimental Section. Graphical representations of the two crystal structures are given in Figure 4. Both show $ReO_3$-like slabs, which are four octahedra wide for the $m = 4$ phase and seven for the phase at $m = 7$. These slabs are linked by phosphate tetrahedra. In both structures the $[MO_6]$ octahedra joining the $ReO_3$-like slabs together are linked to three $[PO_4]$ tetrahedra and they are exclusively occupied by tungsten. These are sites $M2$ in the $m = 4$ phase and $M3$ in the $m = 7$ phase (see Table 4 and Table 5; numbering of atom sites as in the original papers on the pure tungsten MPTBs). In contrast, $[MO_6]$ with only one or no adjacent phosphate group are partly occupied by rhodium. For the $m = 7$ phase even a systematic increase of $Rh^{3+}$ occupancy with increasing distance from the phosphate tetrahedra (from the interface between the $ReO_3$-like slabs) is observed. This cation ordering is rather surprising since valence sum considerations would suggest just the opposite ordering scheme for $Rh^{3+}/W^{6+}$, as is shown by the following considerations along the lines of Paulings rules and Browns equal valence rule.[27] In the crystal structures of the monophosphate tungsten bronzes all oxygen atoms are twofold coordinated (P + W, P + Rh, W + W, W + Rh, Rh + Rh). Assuming ideal valence distribution within the coordination polyhedra $[PO_4]$ ($v_{P\text{-}O} = 5/4$), $[WO_6]$ ($v_{W\text{-}O} = 6/6$), and $[RhO_6]$ ($v_{Rh\text{-}O} = 3/6$) leads to "overbonded" oxygen when coordinated by P + W ($\Sigma v_O = 9/4$). For W + W ($\Sigma v_O = 12/6$), P + Rh ($\Sigma v_O = 7/4$), W + Rh ($\Sigma v_O = 9/6$), Rh + Rh ($\Sigma v_O = 6/6$) the valence sum for oxygen drops from ideal to strongly "underbonded". Allowing slight alteration of interatomic distances would result in some relaxation.[28] However, exchanging tungsten by rhodium in $[MO_6]$ octahedra linked to phosphate would already avoid all unfavorable valence sums for oxygen, i.e. those in contrast to *Paulings* rule of preservation of local electroneutrality.[27] Yet, this is not observed. One explanation might lay in an additional contribution to lattice energy from charge density modulation along the crystallographic $c$-axis in these structures. In other words, slabs with over bonded and under bonded oxygen (surplus of positive and negative charges, respectively) would stack along the crystallographic $c$-axis.

**Table 5.** $(Rh_{2/21}W_{19/21}O_3)_{14}(PO_2)_4$. Atomic coordinates and isotropic displacement parameters.

| Atom | $x$ | $y$ | $z$ | $s.o.f.$ | $U_{eq}$ [Å$^2$] |
|---|---|---|---|---|---|
| W1 | 0 | 0.5 | 0 | 0.822(16) | 0.0222(5) |
| Rh1 | 0 | 0.5 | 0 | 0.178(16) | 0.0222(5) |
| W2 | −0.0011(4) | 0.16144(13) | 0.11289(3) | 0.954(12) | 0.0146(4) |
| Rh2 | −0.0011(4) | 0.16144(13) | 0.11289(3) | 0.046(12) | 0.0146(4) |
| W3 | −0.0001(3) | 0.00523(11) | 0.32958(2) | 1 | 0.0088(3) |
| W4 | 0.0020(5) | 0.32824(14) | 0.44491(3) | 0.875(13) | 0.0200(4) |
| Rh4 | 0.0020(5) | 0.32824(14) | 0.44491(3) | 0.125(13) | 0.0200(4) |
| P1 | 0.506(2) | 0.3156(7) | 0.29117(17) | 1 | 0.0084(9) |
| O1 | 0.553(4) | 0.018(6) | 0.0033(18) | 0.5 | 0.010(7) |
| O2 | 0.540(4) | 0.158(2) | 0.5602(6) | 1 | 0.019(4) |
| O3 | 0.039(4) | 0.167(2) | 0.3847(6) | 1 | 0.021(4) |
| O4 | 0.038(4) | 0.012(3) | 0.1772(6) | 1 | 0.024(4) |
| O5 | 0.485(6) | 0.381(2) | 0.2375(6) | 1 | 0.023(3) |
| O6 | 0.206(5) | 0.133(4) | 0.4713(9) | 1 | 0.039(6) |
| O7 | 0.709(4) | 0.212(4) | 0.4725(8) | 1 | 0.030(5) |
| O8 | 0.301(4) | 0.043(3) | 0.0871(7) | 1 | 0.019(4) |
| O9 | 0.795(4) | -0.028(3) | 0.0892(8) | 1 | 0.025(4) |
| O10 | 0.286(4) | 0.312(3) | 0.1476(8) | 1 | 0.025(5) |
| O11 | 0.780(4) | 0.364(3) | 0.1491(7) | 1 | 0.018(4) |
| O12 | 0.229(3) | 0.227(3) | 0.3022(7) | 1 | 0.018(4) |
| O13 | 0.694(4) | 0.157(3) | 0.2979(8) | 1 | 0.021(4) |

All crystals of $(Rh_{1/9}W_{8/9}O_3)_{12}(PO_2)_4$ ($m = 6$) selected for SXRD structure analysis showed diffuse streaks in sections of the reciprocal space (see Figure S10). No reasonable integration of the reflections was possible. We relate this problem to the presence of severe stacking faults and variable thickness of the $ReO_3$-like slabs.

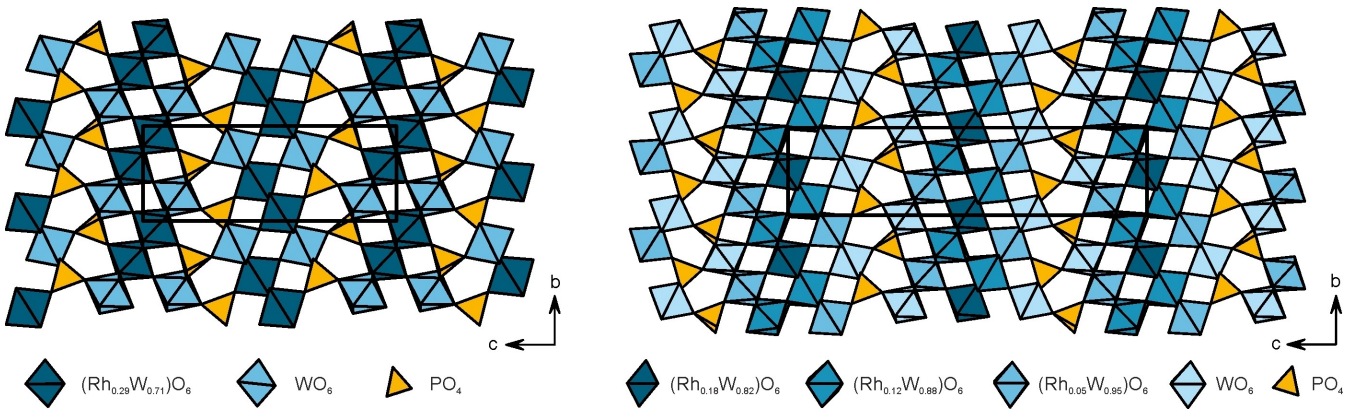


**Figure 4.** Crystal structures of $(Rh_{1/6}W_{5/6}O_3)_8(PO_2)_4$ (left) and $(Rh_{2/21}W_{19/21}O_3)_{14}(PO_2)_4$ (right) with schematic coordination polyhedra. Projections along [100]; dark grey: phosphate tetrahedra; grey: $WO_6$ octahedra; light grey: octahedra $MO_6$ with mixed occupancy Rh/W (graphics software DIAMOND v.4.5.1.[26])

### Electron microscopic investigation

SAED pattern and HRTEM images taken from crushed crystals of $(Rh_{0.15}W_{0.85}O_3)_8(PO_2)_4$ and $(Rh_{0.07}W_{0.93}O_3)_{14}(PO_2)_4$ are displayed in Figure 5. The lattice parameters derived from both SAED patterns accord well with the values obtained from XRD. No hints were found for the presence of superstructures.

The HRTEM images are in agreement with the structure models deduced from SXRD refinement, as it can be seen from overlaying a structural image based on coordination polyhedra (Figure 5). The characteristic fish-bone pattern with rows of $ReO_3$-like slabs and phosphate groups in between are nicely matched. A prominent characteristic of these MPTB structures are the pentagonal tunnels, which are formed between the $ReO_3$-slabs and phosphate groups and display a better white-contrast every second time along [001]. In previous electron-microscopic studies this effect was also observed and investigated. The contrast in MPTB's is very sensitive to crystal tilting near [100] and the crystal thickness.[29] The varying contrast therefore can be explained with a slight misalignment to the zone axis [100] and an unfavorable crystal size.

Images taken with lower magnifications show highly ordered $ReO_3$-like slabs with equal thickness, therefore, providing no hints on stacking faults. This result disagrees with the observation, that the intensities of the reflections (0 0 2) and (0 0 4) (see Tables S4–S7 and Figures S1–S4) calculated from SXRD data differ from the observed intensities of the XRPD data. It is also in contrast to the observation of significant diffuse scattering observed by SXRD for all (Rh,W)-MPTB. Several explanations are possible: Stacking faults occur in some crystals only and are not seen in the areas investigated by HRTEM or the ratio of rhodium/tungsten differs between $ReO_3$-like slabs within a crystal.

### Electronic spectra and magnetic behavior of the (Rh,W)-MPTB

Powders of the (Rh,W)-MPTBs ($m = 4$ and 7) are dark green in contrast to the orange-yellow of $Rh(PO_3)_3$ (*C*-type; $[Rh^{III}O_6]$ chromophore), which we discuss here as reference material. The color difference is in line with powder reflectance measurements of the three compounds shown in Figure 6. For $Rh(PO_3)_3$ the two strong absorption bands at 21500 $cm^{-1}$ and 28000 $cm^{-1}$ can be assigned to the ligand field transitions $^1A_1 \rightarrow {}^1T_{1g}$ and $^1A_{1g} \rightarrow {}^1T_{2g}$ of the octahedral $[Rh^{III}O_6]$ chromophore. Graphical evaluation according to Tanabe and Sugano[30] results in $B = 430$ $cm^{-1}$ and $\Delta = 23200$ $cm^{-1}$. These values are in good agreement with those determined for the $[Rh^{III}F_6]$ chromophore in $K_3RhF_6$ ($B = 460$ $cm^{-1}$, $\Delta = 22300$ $cm^{-1}$).[31] In contrast to $Rh(PO_3)_3$ and $K_3RhF_6$ the (Rh,W)-MPTBs show a broad absorption band in the NIR/vis ranging from 5000 $cm^{-1}$ to 14000 $cm^{-1}$ and a second in the vis/UV ranging from 19000 $cm^{-1}$ to 29000 $cm^{-1}$ (see Figure 6). The minimum around 17000 $cm^{-1}$ readily explains their green color. The absorption in the NIR/vis is reminiscent to those observed for blue heteropolytungstates,[32] mixed-valent tungsten oxides, e.g. $WO_{3-\delta}$,[33] $W_{20}O_{58}$[34] or for electrochromic tungsten bronzes, e.g. $Na_xWO_3$[35] and might thus point to the presence of some $W^{5+}$ besides $W^{6+}$ and $Rh^{3+}$. The ligand-field transitions for the $[Rh^{III}O_6]$ chromophore are not resolved in the (Rh,W)-MPTBs, most likely they are superimposed by LMCT ($O^{2-} \rightarrow W^{6+}$).

Angular overlap modelling (AOM)[36] has been used to reproduce the *d*-electron energy levels of $Rh^{3+}$ in $Rh(PO_3)_3$. For the AOM calculations the PC program CAMMAG[37] in a modified version[38] was used. Best fit AOM parameters obtained from the optical spectrum of $Rh(PO_3)_3$ are $B = 490$ $cm^{-1}$ ($\beta = 0.80$), $C = 1960$ $cm^{-1}$, $\zeta = 1408$ $cm^{-1}$, $e_\sigma(Rh–O) \sim d(Rh–O)^{-5.0}$ and $e_\sigma(Rh–O)_{max} = 11300$ $cm^{-1}$. Isotropic $\pi$-interaction Rh–O was assumed to be 1/4 of the corresponding $\sigma$-interaction $\{e_\pi(Rh–O) = 1/4\ e_\sigma(Rh–O)\}$. As can be seen from the comparison in Figure 6, results from AOM match well with the observed energies for the transitions $^1A_{1g} \rightarrow {}^3T_{1g}$, $^1A_{1g} \rightarrow {}^3T_{2g}$, $^1A_{1g} \rightarrow {}^1T_{1g}$, and $^1A_{1g} \rightarrow {}^1T_{2g}$ of the $[Rh^{III}O_6]$ chromophore.

For $Rh^{III}(PO_3)_3$ and the (Rh,W)-MPTBs with the ideal compositions $(Rh^{III}_{1/6}W^{VI}_{5/6}O_3)_8(PO_2)_4$ and $(Rh^{III}_{2/21}W^{VI}_{19/21}O_3)_{14}(PO_2)_4$ one could expect diamagnetic behavior due to the $d^0$ configuration of $W^{6+}$ and the $^1A_{1g}$ electronic ground state of $Rh^{3+}$ ($d^6$, *low-spin*). However, considering a second-order Zeeman effect for

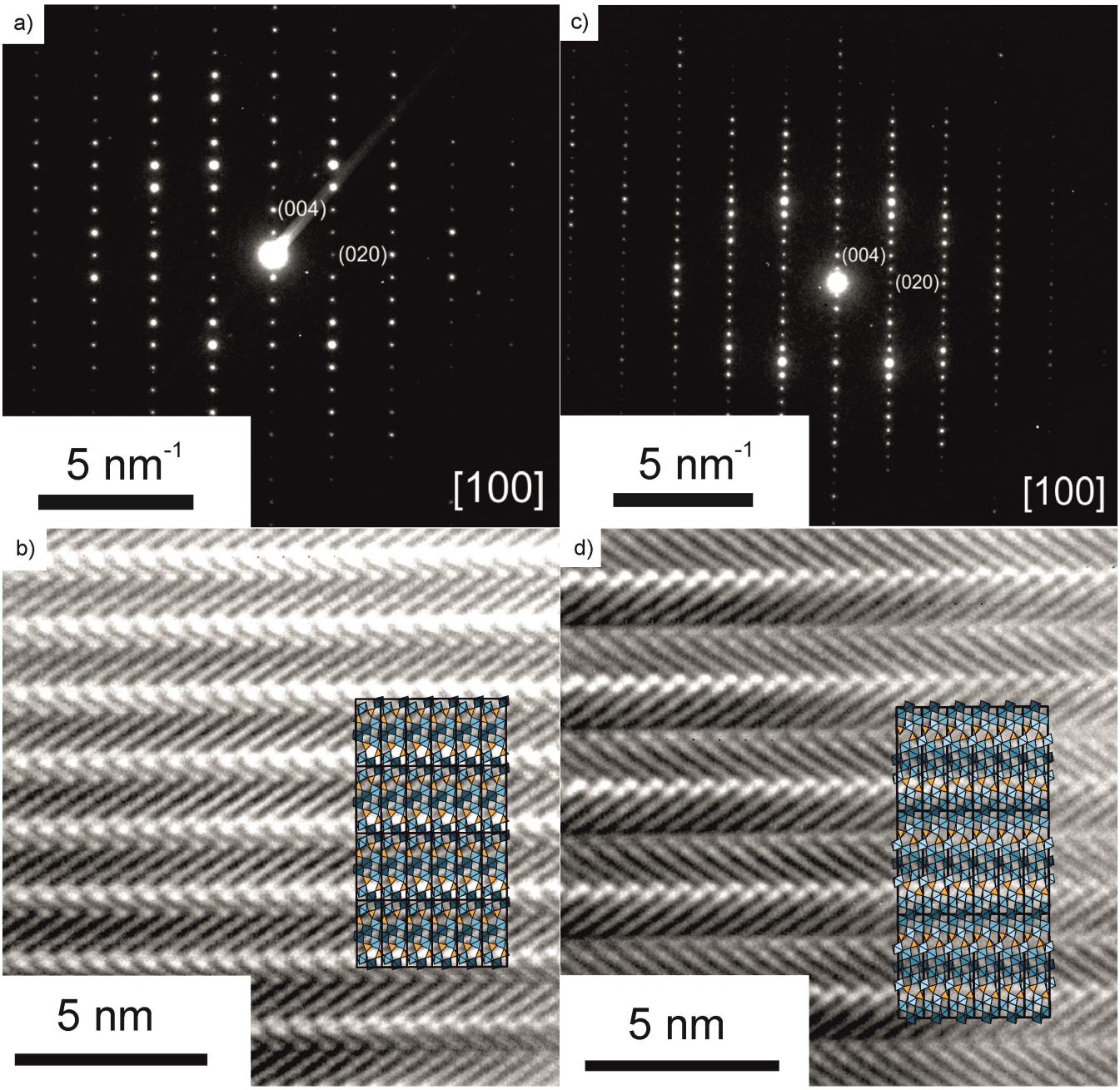


**Figure 5.** Top: Selected area electron diffraction (SAED) pattern of $(Rh_{1/6}W_{5/6}O_3)_8(PO_2)_4$ (a) and $(Rh_{2/21}W_{19/21}O_3)_{14}(PO_2)_4$ (c) in [1 0 0] zone axis orientation. Bottom: Fourier-filtered HRTEM image (CM30 T) of $(Rh_{1/6}W_{5/6}O_3)_8(PO_2)_4$ (b) and $(Rh_{2/21}W_{19/21}O_3)_{14}(PO_2)_4$ (d) in [1 0 0] zone axis orientation with overlaid structure of the MPTBs.

$Rh^{3+}$ would lead to a small magnetic moment independent of temperature (TIP) according to van Vleck's equation.[39] Indeed, this expectation is perfectly met by the temperature independent susceptibility observed for $Rh(PO_3)_3$, $\chi_{TIP} = +100 \cdot 10^{-6}$ emu·mol$^{-1}$ (Figure 7). This value is also in agreement with measurements for $Rh^{3+}$ (e.g. $RhCl_3$: $\chi_{TIP} = +85 \cdot 10^{-6}$ emu·mol$^{-1}$;[40] $Rh_2(SO_4)_3 \cdot 12\ H_2O$: $\chi_{TIP} = +95 \cdot 10^{-6}$ emu·mol$^{-1}$;[40] $[Rh_3O(CH_3COO)_6(py)_3]ClO_4$: $\chi_{TIP} = +280 \cdot 10^{-6}$ emu·mol$^{-1}$;[41] all $\chi$ per formula unit). Furthermore, the results from angular overlap modelling that already matched the excited state energies for the $[Rh^{III}O_6]$ chromophore are fully consistent with the observed TIP for rhodium(III) metaphosphate (Figure 7). In contrast, the (Rh,W)-MPTBs show much higher molar susceptibilities ($\chi_{TIP}(Rh_{1.164}W_{6.836}P_4O_{32}) = +299 \cdot 10^{-6}$ emu·mol$^{-1}$, $\chi_{TIP}(Rh_{1.04}W_{12.96}P_4O_{32}) = +470 \cdot 10^{-6}$ emu·mol$^{-1}$; both obtained from a linear fit to the respective graphs of $\chi_{mol} \cdot T$ vs. $T$ shown in Figure S11, plot of $\mu_{eff}$ vs. $T$ see Figure S12) which cannot be rationalized on basis of the exclusive presence of $[Rh^{III}O_6]$ (Figure 7).

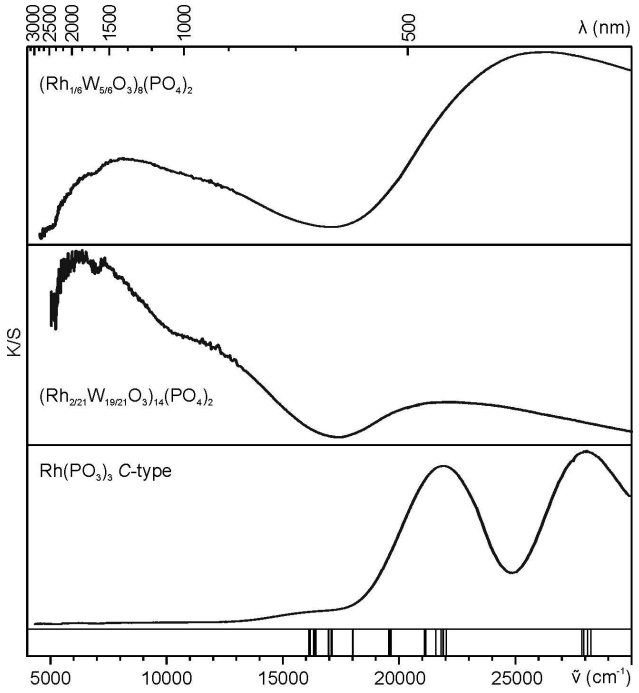


**Figure 6.** Powder reflectance spectra of $(Rh_{1/6}W_{5/6}O_3)_8(PO_2)_4$ (top) and $(Rh_{2/21}W_{19/21}O_3)_{14}(PO_2)_4$ (middle) diluted with $BaSO_4$ (50:50 ratio) in comparison to a spectrum of pure $Rh(PO_3)_3$ *C*-type (bottom). Ticks at the bottom are representing zero-phonon excitations for $Rh(PO_3)_3$ from the best fit angular overlap modelling (AOM; see text).

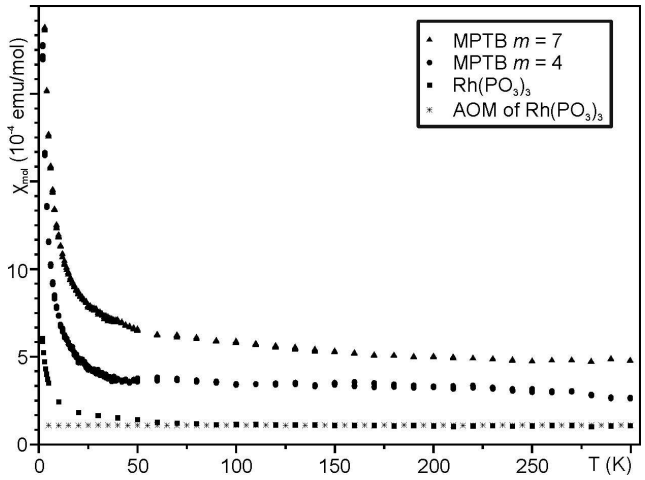


**Figure 7.** Molar (per formula unit) magnetic susceptibilities of $Rh_{1.164}W_{6.836}P_4O_{32}$ ($m=4$), $Rh_{1.04}W_{12.96}P_4O_{32}$ ($m=7$) and $Rh(PO_3)_3$ in a field of $10^4$ G.

Subtracting $\chi_{TIP}(Rh^{3+}) = +100\cdot10^{-6}$ emu·mol$^{-1}$ from $\chi_{mol,\ exp}$ of the (Rh,W)-MPTBs still leaves for both significant contributions to the overall magnetic susceptibility. Two explanations, both related to the presence of $W^{5+}$ ($d^1$ electronic system, $^2T_{2g}$ electronic ground state for the octahedral chromophore $[W^{5+}O_6]$), appear to be possible. Neither would lead to simple Curie-Weiss-behavior. Magnetic behavior of sodium tungsten bronzes $Na_xWO_3$ might serve as comparison.[42] Therein reported susceptibilities, due to the Pauli paramagnetism[43] of delocalized electrons, are far too small to provide a reasonable explanation for the TIP of the (Rh,W)-MPTBs. A second approach for understanding might be based on the paramagnetism of localized electrons in $W^{5+}$. Yet, due to strong spin-orbit coupling and the wide variability of ligand field effects in 5d ions predictions on the paramagnetic behavior of $W^{5+}$ containing compounds are hard to make. Comparison to simple, magnetically well characterized systems (e.g. $CsW^VF_6$[44], $CsW^VCl_6$[45]) suggests a rather high content of up to 50% $W^{5+}$ of the total tungsten content of the (Rh,W)-MPTBs. This seems to be unrealistically high by any means. Given the overall rather small susceptibilities of the (Rh,W)-MPTBs leaves eventually just the assumption of contributions of unidentified paramagnetic impurities as explanation. In this context it is worth noting that magnetic susceptibility data obtained for two batches of the (Rh,W)-MPTB at $m=4$ (powder synthesis and crushed crystals from CVT) were almost identical. Clearly, characterization of the electronic structure of the (Rh,W)-MPTBs requires additional work, which is ongoing.

## Chemical composition of the (Rh,W)-MPTBs

Seemingly, different experimental data (synthesis, SXRD, optical spectroscopy, magnetic measurements) for the (Rh,W)-MPTBs suggest different chemical composition for these phases. Thus, a critical review of these data with respect to the chemical composition of the phases under investigation is justified.

Syntheses based on the ideal compositions (exclusively $Rh^{3+}$ and $W^{6+}$) $(Rh_{1/6}W_{5/6}O_3)_8(PO_2)_4$ (phase at $m=4$) and $(Rh_{2/21}W_{19/21}O_3)_{14}(PO_2)_4$ (phase at $m=7$) led to single phase powder samples according to XRPD analysis of the solid reaction products. By-phases as consequence of deviations in composition will only be observable for an estimated amount higher than 3%wt.

Structure refinements from SXRD data suggest small deviations from the ideal Rh/W ratio with slightly higher tungsten content than expected. Even though there is some correlation between site occupancy factors for Rh/W and the corresponding displacement parameters, we believe that the rhodium content of the two (Rh,W)-MPTBs is indeed slightly lower than expected for the ideal composition. Yet, the composition from SXRD might be regarded as the lower limit of rhodium content. While no hints on stacking faults in the (Rh,W)-MPTBs were obtained from HRTEM and SAED, diffuse scattering observed in SXRD patterns point to such defects which possibly will lead to deviations in stoichiometry.

Color and powder reflectance spectra of the (Rh,W)-MPTBs are strikingly different than what is observed for the perfectly stoichiometric and electronically well-defined metaphosphate $Rh^{III}(PO_3)_3$. Strong bands in the NIR/vis region suggest mixed-valency $W^{5+}/W^{6+}$, yet already less than 1% of $W^{5+}$ would be sufficient to cause such an absorption behavior, as is evidenced by the deep blue color of under-stoichiometric $WO_{3-\delta}$.[33,34]

Magnetic susceptibility data of $(Rh_{1/6}W_{5/6}O_3)_8(PO_2)_4$ and $(Rh_{2/21}W_{19/21}O_3)_{14}(PO_2)_4$ do show, as expected, weak paramagnetism.

Yet, the absolute numbers cannot be rationalized solely based on the TIP expected for $Rh^{3+}$.

Results from EDS analyses (see Table 6) of crystals from CVT seem also to indicate a slightly smaller ratio Rh/W than related to the ideal compositions of the (Rh,W)-MPTBs. Yet, these analyses (including a ZAF correction) overestimate the light elements (phosphorus content) and underestimate heavy elements (Rh, W).

Summarizing these critical considerations, we believe that the obtained (Rh,W)-MPTBs do indeed show a slightly lower ratio Rh/W than that of the "ideal" compositions. Clearly, these phases do contain a small but significant amount of $W^{5+}$. Structural investigations did not give any hint on variations of the metal/phosphorus ratio in the (Rh,W)-MPTBs.

## Conclusions

In extension of previous work it is shown that in MPTBs $(WO_3)_{2m}(PO_2)_4$ substitution of $W^{5+}$ by appropriate combinations of $Rh^{3+}$ (or $Ir^{3+}$) and $W^{6+}$ is possible. Thus, new mm-MPTBs with the ideal compositions $(Rh_{1/6}W_{5/6}O_3)_8(PO_2)_4$, $(Rh_{1/9}W_{8/9}O_3)_{12}(PO_2)_4$, $(Rh_{2/21}W_{19/21}O_3)_{14}(PO_2)_4$ ($m = 4$, 6, 7) and $(Ir_{1/6}W_{5/6}O_3)_8(PO_2)_4$ (only $m = 4$) were obtained.

Solution combustion synthesis with subsequent annealing of the combustion products provides access to these new mm-MPTBs. Furthermore, the progress of phase formation during annealing (amorphous→$ReO_3$-related phase→two-phase off-equilibrium mixtures→mm-MPTB equilibrium phase) allows a unique glimpse into the processes related to stepwise crystallization and equilibration of an amorphous, solid starting material. Thermodynamically metastable mixed-metal phosphates with $ReO_3$-related XRPD pattern were established as single-phase intermediates. Their formation emphasizes the hitherto not recognized versatility of SCS for synthesis of thermodynamically metastable solids.

Thermal decomposition behavior of the (Rh,W)-MPTBs is in agreement with only a rather small stabilization of these phases relative to $W_2O_3(PO_4)_2$, $WO_3$, and $Rh_2O_3$ and the thermal decomposition products thereof $WO_3$, Rh and gaseous $P_4O_{10}$. Therefore, crystallization of the (Rh,W)-MPTBs by chemical vapor transport (transport agent chlorine) is possible.

Structure refinement of the (Rh,W)-MPTBs at $m = 4$ and 7 show cation distributions Rh/W that are in contrast to Paulings electroneutrality rule. An overall stabilization due to alternating layers with small positive/negative charges could be a reason.

**Table 6.** Ideal and analytical composition of "$(Rh_{1/6}W_{5/6}O_3)_8(PO_2)_4$" ($m = 4$) and "$(Rh_{2/21}W_{19/21}O_3)_{14}(PO_2)_4$" ($m = 7$).

| | $m = 4$ | | | $m = 7$ | | |
|---|---|---|---|---|---|---|
| | Rh [%] | W [%] | P [%] | Rh [%] | W [%] | P [%] |
| ideal composition | 11.11 | 55.56 | 33.33 | 7.41 | 70.37 | 22.22 |
| SXRD | 9.7(1) | 57.0(1) | 33.33 | 5.8(5) | 72.(5) | 22.22 |
| EDS (REM)[a] | 11.0(8) | 50(2) | 39(3) | 7.1(6) | 67(3) | 26(2) |

[a] Area measurement of single crystals

Optical spectra and magnetic behavior of the obtained (Rh,W)-MPTBs suggest mixed-valency $W^{5+/6+}$ and, as a consequence, a small tungsten surplus with respect to the ideal formulae. Eventually, in the course of our investigation on the (Rh,W)-MPTBs a ligand field analysis for *C*-type $Rh(PO_3)_3$ based on powder reflectance and magnetic measurements has been carried out as reference for the chromophore $[Rh^{III}O_6]$.

## Experimental Section

***X-ray powder diffraction***. Powder diffraction pattern for phase identification and purity control were recorded at ambient temperature using an imaging plate (*IP*) Guinier camera (HUBER G670, Cu-K$\alpha_1$ radiation, $\lambda = 1.54059$ Å, 15 minutes exposure time in the angular range $4° \leq 2\theta < 100°$). The observed powder diffraction pattern of $(Rh_{1/6}W_{5/6}O_3)_8(PO_2)_4$, $(Rh_{2/21}W_{19/21}O_3)_{14}(PO_2)_4$, $(Rh_{1/9}W_{8/9}O_3)_{12}(PO_2)_4$ and $(Ir_{1/6}W_{5/6}O_3)_8(PO_2)_4$ are compared to simulations which are based on the data from single crystal structure analysis or isotypic compounds with matched lattice parameters and a suitable chemical composition (Figure 1). Tables containing the assigned reflections from the Guinier photograph are available online as Supplementary Material (Table S1–4).

***Single-crystal X-ray diffraction***. Suitable crystals of $(Rh_{1/6}W_{5/6}O_3)_8(PO_2)_4$ and $(Rh_{2/21}W_{19/21}O_3)_{14}(PO_2)_4$ were selected carefully under a polarizing microscope and glued to glass fibers. Diffraction data (graphite-monochromated Mo-K$\alpha$1 radiation; $\lambda = 0.71073$ Å) were collected using a Bruker Nonius κ-CCD area-detector diffractometer (BRUKER AXS B.V., Delft, Netherlands) which was controlled by the Nonius "Collect" software.[46] For data processing the software package "HKL2000: Denzo & Scalepack" was employed.[47] A semi-empirical absorption correction based on multiscans was applied to the diffraction data using the program package Platon.[48]

**$(Rh_{1/6}W_{5/6}O_3)_8(PO_2)_4$**: Starting parameters for the structure refinement were obtained by the dual space structure solution algorithm (SHELXT[49]) and refined with a full-matrix least-squares technique (SHELX-97,[50] WinGX[51]). Space group $P2_12_12_1$ as for the pure tungsten MPTB $(WO_3)_8(PO_2)_4$[14] was assumed. The two independent metal sites were in a first step treated as fully occupied by tungsten. Site W1 (notation as given in literature[14] for $(WO_3)_8(PO_2)_4$) showed in contrast to W2 a rather large displacement parameter. In the next refinement step for site M1 mixed occupancy W/Rh was assumed. Refinement was carried out using the EXYZ and EADP constraints for W/Rh on site M1 and assuming full occupancy. No hint was found for mixed occupation of site M2. The refinement led to 1.17 Rh and 6.83 W in the unit cell instead of 1.33 Rh and 6.67 W, as it was expected from charge neutrality ($Rh^{3+}$, $W^{6+}$) considerations. It should be noted in this context that any effort to constrain the ADPs for sites M1 and M2 yielded significantly higher rhodium contents in the unit cell (e.g. 1.75 Rh; 6.25 W) but drastically worse residuals. Eventually, anisotropic displacement parameters could be introduced for sites M1 and M2. Phosphorus and oxygen could only be refined isotropically, due to occurrence of physically meaningless ("n.p.d.") atomic displacement parameters. Racemic twinning was accounted for and led to the volume ratio V1/V2 = 0.52(5). The remaining highest electron density (1.82 $e^-/Å^3$) was found close to O8 with similar residual electron density close to other oxygen sites. We attribute these maxima to the limitations of the isotropic refinement. The deepest minimum in electron density (−2.78 $e^-/Å^3$) was found close to site M1. It is interpreted as an effect of discontinuation of the Fourier series. The flaws in this refinement

(despite acceptable residuals R1 = 3.2 %, wR2 = 7.4 %) mirror those reported for many other refinements of MPTB type compounds.

**$(Rh_{2/21}W_{19/21}O_3)_{14}(PO_2)_4$:** Starting parameters for the structure refinement were obtained by Direct Methods (SHELX-97[50]). Space group $P2_1/n$ as for the isotypic MPTB $(WO_3)_{14}(PO_2)_4$[16] as assumed in the refinement (full-matrix least-squares refinement: SHELX-97,[50] WinGX[51]). Assuming full occupancy of the metal sites, three (W1, W2, W4) out of four tungsten sites showed unusually high isotropic displacement parameters. Therefore, except for site W3, mixed occupancy Rh/W was introduced using the EXYZ and EADP constraints for each of the three sites. Even after accounting for twinning (mirror plane perpendicular to the crystallographic *c*-axis, as reported in literature for $(WO_3)_{14}(PO_2)_4$[25]) refinement of anisotropic displacement parameters was only possible for the metal and phosphorus sites. Eventually, for oxygen atom O1 occupying the Wyckhoff site 2*d* a split position with half occupancy of the general site 4*e* was introduced. From the refinement 1.04 rhodium and 12.96 tungsten in the unit cell were obtained in contrast to 1.33 Rh and 12.67 W for the ideal composition. The value of $R_{int}$ = 0.12 indicates low quality of the diffraction data, which is typical for many refinements of MPTB structures.

***Electron microscopic investigation***. TEM images were conducted on a FEI-Philips CM30 T/$LaB_6$ microscope operated at 300 kV and equipped with a Gatan CCD for image recording. The samples were prepared by suspending a little amount in cyclohexane using an ultrasonic bath, applying a drop of the dispersion on a holey carbon film reinforced by a copper grid and evaporating the solvent. Digital TEM images were processed using the Gatan Digital Micrograph software.[52]

To get an image along the [100] zone axis, a suitable crystal was tilted along dynamic electron diffraction ("Kikuchi-lines") towards a simulated pattern. A diffraction pattern was taken and evaluated to confirm the zone axis, afterwards a HRTEM image was prepared. The HRTEM images were Fourier filtered using the Gatan Microscopy Suite. After an analysis of the real space distances, a model from the SXRD solution could be superimposed over the HRTEM image. EDS analysis were carried out on a Hitachi SU3800 with a tungsten cathode operated at 10 kV. For quatification the EDAX detector "Octane Elect Super EDS" (peltier element cooling) and a ZAF correction were used. Results were obtained as mean values from several examined single-crystals.

***Electronic absorption spectroscopy***. Powder reflectance spectra were measured at room temperature using modified CARY-14 (UV-region) and CARY-17 (vis/NIR-region) spectrophotometers (OLIS, USA) equipped with integrating (Ulbricht) spheres. Four different setups for measurement (step width, band width, scan rate, detector) were applied to cover the range from 5000 $cm^{-1}$ to 40000 $cm^{-1}$. In the UV range (200 nm–600 nm) 800 data points (step width 0.5 nm, scan rate 1 nm · $sec^{-1}$, band width 0.6 nm), in the visible range (300 nm–900 nm) 600 data points (step width 1.0 nm, scan rate 1 nm · $sec^{-1}$, band width 1.2 nm) and in the near-infrared range (600 nm–2200 nm) 500 data points (step width 4 nm, scan rate 2 nm · $sec^{-1}$, band · width 5 nm) were recorded. For detection in the UV/vis region a photomultiplier detector (PMT) was used, in case of the vis region with an aperture width of 0.06 nm. In the near-infrared region a semiconducting lead(II)sulfide detector with variant gap widths (1.4 nm–2.2 nm) was utilized. The spectra are represented as a ration of *K/S* vs. wavenumber (*Kubelka-Munk* function).[53]

***Magnetic measurements***. Magnetic measurements were carried out using a vibrating sample magnetometer (Quantum design, USA). The strength of the external magnet field was $10^4$ Oe in the temperature range from 2 K to 300 K. Magnetic susceptibilities were measured during cooling and heating. At each temperature step a series of ten measurements were taken. Only close to ambient temperature, slight differences between the data obtained on cooling or heating were observed. The susceptibility data shown in Figure 7 have been corrected for capsule and diamagnetic contributions.[54] Furthermore, a low content of ferromagnetic impurity was corrected with a Honda-Owen plot. Therefore, measurements with a different external field (0 to 20000 Oe) were conducted at 150 and 300 K for all samples. All susceptibilities are given for 1 mole (formula unit) of the compound. In case of the MPTBs the sum formula according to SXRD was used.

Deposition Numbers 2062902 (for $Rh_{0.15}W_{0.85}O_3)_8(PO_2)_4$ (phase at $m$=4)), and 2062903 (for $Rh_{0.07}W_{0.93}O_3)_{12}(PO_2)_4$ (phase at $m$=7)) contain the supplementary crystallographic data for this paper. These data are provided free of charge by the joint Cambridge Crystallographic Data Centre and Fachinformationszentrum Karlsruhe Access Structures service www.ccdc.cam.ac.uk/structures.

## Acknowledgements

*We thank Norbert Wagner for magnetic measurements, Nils Kannengießer for measurements of the UV/vis/NIR spectra and Volker Bendisch (all of Inorganic Chemistry at Bonn University) for photographs of the single-crystals. Funding by BASF SE, cooperative work and discussions throughout the cooperation project "PGM Phosphates" are gratefully acknowledged. Open access funding enabled and organized by Projekt DEAL.*

## Conflict of Interest

The authors declare no conflict of interest.

**Keywords:** Equilibrium relations · MPTB · Rhodium · Iridium · Solid-state chemistry · Solid-state structure

[1] a) S. A. Schunk, S. Titlbach, F. Rosowski, R. Mueller, C. Schulz, J. Xie, S. Schaefer, P. Loeser, K. Wittich, M. Weber, R. Glaum, World Patent WO 2020120755, **2020**; b) C. A. Welker-Nieuwoudt, F. Rosowski, M. Goebel, R. Glaum, C. R. Roy, G. Hautier, D. Waroquiers, R. Naumann d'Alnoncourt, V. Strempel, S. Linke, Patent DE 10 2016 007628A1, **2016**.
[2] R. K. Grasselli, *Top. Catal.* **2001**, *15*, 93–101.
[3] P. Rittner, R. Glaum, *Z. Kristallogr.* **1994**, *209*, 162–169.
[4] K. Panagiotidis, R. Glaum, W. Hoffbauer, J. Weber, J. Schmedt auf der Günne, *Z. Anorg. Allg. Chem.* **2008**, *634*, 2922–2932.
[5] F. Wöhler, *The Philosophical Magazine* **1825**, *66*, 263–269.
[6] a) M. Greenblatt, *Int. J. Mod. Phys. B* **1993**, *7*, 3937–3971; b) B. Domengès, F. Studer, B. Raveau, *Mater. Res. Bull.* **1983**, *18*, 669–676.
[7] E. Wang, M. Greenblatt, *J. Solid State Chem.* **1987**, *68*, 38–44.
[8] C. Hess, C. Schlenker, G. Bonfait, T. Ohm, C. Paulsen, D. Dumas, Z. Teweldemedhin, M. Greenblatt, J. Marcus, M. Almeida, *Solid State Commun.* **1997**, *104*, 663–668.
[9] P. Roussel, O. Pérez, Ph. Labbé, *Acta Crystallogr.* **2001**, *B57*, 603–632.
[10] S. C. Roy, W. Assenmacher, T. Linden, L. Esser, W. Mader, R. Glaum, *Z. Naturforsch.* **2016**, *B71*, 543–552.
[11] a) A. Varma, A. S. Mukasyan, A. S. Rogachev, K. V. Manukyan, *Chem. Rev.* **2016**, *116*, 14493–14586; b) K. C. Patil, M. S. Hegde, T. Rattan, S. T. Aruna in *Chemistry of nanocrystalline oxide materials*, World Scientific, Singapore, **2008**, vol. 1, pp. 42–60.
[12] S. C. Roy, B. Raguž, W. Assenmacher, R. Glaum, *Solid State Sci.* **2015**, *49*, 18–28.
[13] G. Meyer, J. Soose, *SOS, University of Gießen* **1980**.

[14] J. P. Giroult, M. Goreaud, P. Labbé, B. Raveau, *Acta Crystallogr.* **1981**, *B37*, 2139–2142.
[15] P. Labbe, M. Goreaud, B. Raveau, *J. Solid State Chem.* **1986**, *61*, 324–331.
[16] P. Roussel, P. Labbé, D. Groult, B. Domengès, H. Leligny, D. Grebille, *J. Solid State Chem.* **1996**, *122*, 281–290.
[17] O. Yamaguchi, D. Tomihisa, H. Kawabata, K. Shimizu, *J. Am. Ceram. Soc.* **1987**, *70*, 94–96.
[18] H. Görzel, R. Glaum, *Z. Anorg. Allg. Chem.* **1996**, *622*, 1773–1780.
[19] H. Putz, *MATCH! v. 3.6.1.115 (Crystal impact), Bonn*, **2003–2018**.
[20] H. Schaefer, V. P. Orlovskii, M. Wiemeyer, *Z. Anorg. Allg. Chem.* **1972**, *390*, 13–24.
[21] M. Binnewies, R. Glaum, M. Schmidt, P. Schmidt in *Chemische Transportreaktionen*, Walter de Gruyter, Berlin, **2011**, vol. 1, pp. 1–330.
[22] V. Plies, T. Kohlmann, R. Gruehn, *Z. Anorg. Allg. Chem.* **1989**, *568*, 62–72.
[23] O. Trappe, R. Glaum in *CVTrans V. 4.999 beta*, University of Gießen, **1996–1997**.
[24] R. H. Blessing, *Acta Crystallogr.* **1995**, *A51*, 33–38.
[25] P. Roussel, P. Labbe, D. Groult, *Acta Crystallogr.* **2000**, *B56*, 377–391.
[26] H. Putz, K. Brandenburg, *Diamond v. 4.5.1 (Crystal impact), Bonn* **1997–2018**.
[27] L. Pauling, *J. Am. Chem. Soc.* **1929**, *51*, 1010–1026.
[28] I. D. Brown, *Chem. Rev.* **2009**, *109*, 6858–6919.
[29] B. Domengès, M. Hervieu, B. Raveau, R. J. D. Tilley, *J. Solid State Chem.* **1984**, *54*, 10–28.
[30] Y. Tanabe, S. Sugano, *J. Phys. Soc. Jpn.* **1954**, *9*, 753–766.
[31] H. H. Schmidtke, *Z. Phys. Chem.* **1964**, *40*, 96–108.
[32] a) M. T. Pope, Y. Jeannin, M. Fournier, *Heteropoly and Isopoly Oxometalates*, in Inorganic Chemistry Concepts, vol. 8, 101–116, Springer, Berlin, **1983**; b) Jy. Niu, B. Z. Shan, X. Z. You, *Trans. Metal Chem.* **1999**, *24*, 108–114.
[33] R. D. Tilley in *Colour and the optical properties of Materials*, John Wiley & Sons, Ltd, New Jersey, **2000**, 211–213.
[34] M. Weil, W.-D. Schubert, *The beautiful colors of tungsten oxides*, ITIA Newsletter **2013**.
[35] P. G. Dickens, R. M. P. Quilliam, M. S. Whittingham, *Mater. Res. Bull.* **1968**, *3*, 941–949.
[36] a) B. N. Figgis, M. A. Hitchman in *Ligand field theory and its applications*, Wiley-VCH, New York, **2000**, vol. 1, pp. 53–82; b) D. E. Richardson, *J. Chem. Educ.* **1993**, *70*, 372–80; c) C. K. Jorgensen, R. Pappalardo, H.-H. Schmidtke, *J. Phys. Chem.* **1963**, *39*, 1422–1430.
[37] a) M. Gerloch in *Magnetism and ligand-field analysis*, Cambridge Univ. Press, Cambridge, **2009**, pp. 24–32; b) M. Gerloch, D. A. Cruse, J. E. Davies, M. J. Harding, D. J. Mackey, R. F. McMeeking, *"CAMMAG" a Fortran-program, University of Cambridge* **1975**.
[38] M. Riley, *CAMMAG for PC, v.4.0* **1997**, University of Queensland, St. Lucia.
[39] J. H. van Vleck in *Electric and Magnetic Susceptibilities*, Oxford University Press, Oxford, **1932**, 232–235.
[40] J. Gavis, M. J. Sienko, *J. Am. Chem. Soc.* **1955**, *77*, 4983–4984.
[41] H. Kobayashi, N. Uryû, A. Tokiwa, T. Yamaguchi, Y. Sasaki, T. Ito, *Bull. Chem. Soc. Jpn.* **1992**, *65*, 198–202.
[42] J. D. Greiner, H. R. Shanks, D. C. Wallace, *J. Chem. Phys.* **1962**, *36*, 772–776.
[43] W. Pauli, *Z. Phys. A* **1927**, *41*, 81–102.
[44] G. B. Hargreaves, R. D. Peacock, *J. Chem. Soc.* **1958**, 3776–3779.
[45] W. Eichler, H.-J. Seifert, *Z. Anorg. Allg. Chem.* **1977**, *431*, 123–133.
[46] *"Collect" data collection software*, Nonius B. V., **1999**.
[47] Z. Otwinowski, W. Minor, *Methods Enzymol.* **1997**, *276*, 307–326.
[48] A. L. Spek, *J. Appl. Crystallogr.* **2003**, *36*, 7–13.
[49] G. M. Sheldrick, *Acta Crystallogr. Sect. A* **2014**, *70*, C1437.
[50] G. M. Sheldrick in *SHELX-97 (Release 97–2)*, University of Göttingen, **1998**.
[51] L. J. Farrugia, *J. Appl. Crystallogr.* **1999**, *32*, 837–838.
[52] P. Stadelmann, "JEMS", can be found under http://cimewww.epfl.ch/people/stadelmann/jemsWebSite/jems.html.
[53] a) P. Kubelka, F. Munk, *Z. Tech. Phys.* **1931**, *12*; b) G. Kortüm in *Reflectance Spectroscopy. Principles, Methods, Applications*, Springer, Berlin, **1969**, vol. 1, pp. 170–216.
[54] G. A. Bain, J. F. Berry, *J. Chem. Educ.* **2008**, *85*, 532–536.
[55] M. Binnewies, E. Milke, *Thermodynamic data of elements and compounds*, Wiley VCH, Weinheim **1998**.

Manuscript received: January 19, 2021
Revised manuscript received: March 10, 2021
Accepted manuscript online: March 12, 2021